Native Ultrastructure of the Red Cell Cytoskeleton by Cryo-Electron Tomography

Andrea Nans,[†‡] Narla Mohandas,[§] and David L. Stokes[†¶*]

[†]Skirball Institute of Biomolecular Medicine, Department of Cell Biology, New York University School of Medicine, New York, New York; [‡]Structural Biology Graduate Program, New York University School of Medicine, New York, New York; [§]The Red Cell Physiology Laboratory, The New York Blood Center, New York, New York; and [¶]New York Structural Biology Center, New York, New York

ABSTRACT Erythrocytes possess a spectrin-based cytoskeleton that provides elasticity and mechanical stability necessary to survive the shear forces within the microvasculature. The architecture of this membrane skeleton and the nature of its intermolecular contacts determine the mechanical properties of the skeleton and confer the characteristic biconcave shape of red cells. We have used cryo-electron tomography to evaluate the three-dimensional topology in intact, unexpanded membrane skeletons from mouse erythrocytes frozen in physiological buffer. The tomograms reveal a complex network of spectrin filaments converging at actin-based nodes and a gradual decrease in both the density and the thickness of the network from the center to the edge of the cell. The average contour length of spectrin filaments connecting junctional complexes is 46 ± 15 nm, indicating that the spectrin heterotetramer in the native membrane skeleton is a fraction of its fully extended length (~190 nm). Higher-order oligomers of spectrin were prevalent, with hexamers and octamers seen between virtually every junctional complex in the network. Based on comparisons with expanded skeletons, we propose that the oligomeric state of spectrin is in a dynamic equilibrium that facilitates remodeling of the network as the cell changes shape in response to shear stress.

INTRODUCTION

Erythrocytes are subject to high amounts of shear stress as they traverse the narrow capillaries of the microvasculature and transit from the cords to the sinuses of the spleen. A specialized membrane skeleton is designed to accommodate this stress by facilitating large, reversible deformations of the red cell while maintaining a constant internal volume and constant membrane surface area (1–3). Spectrin, the most abundant protein in this membrane skeleton, forms long, flexible heterodimers through antiparallel, lateral association of α- and β-chains. Symmetric head-to-head interactions between the N-terminus of α-spectrin and the C-terminus of β-spectrin produce bipolar heterotetramers. The tails of the heterotetramer bind the junctional complex composed of F-actin, protein 4.1, and actin-binding proteins dematin, adducin, tropomyosin, and tropomodulin. By attaching several spectrin heterotetramers to each junctional complex, a network is constructed that covers the entire membrane surface of the red cell. This network is tethered to the cell membrane at two sites, one mediated by ankyrin that couples spectrin to Band 3 and the other mediated by protein 4.1 that couples the junctional complex to glycophorin C. Thus, the structural integrity of the erythrocyte membrane is dependent on the horizontal linkages within the spectrin-based network and on the vertical linkages between this network and integral membrane proteins (4). The physiological importance of this assembly is highlighted by the effects of mutations in various skeletal components, which give rise to several hereditary red blood cell disorders characterized by membrane fragmentation, hemolysis, and, ultimately, anemia (1,5).

Structural models for the membrane skeleton suggest that the spectrin network is highly malleable and can adopt expanded and nonexpanded forms. An early model based on negative stain electron microscopy depicts a lattice-like network of fully extended spectrin heterotetramers (~194 nm long (6)) with five to six tails intersecting at each junctional complex (7–10). Although these studies were the first to provide high-resolution information on the structural organization of the membrane skeleton, this single-layered, expanded form is unlikely to represent the network organization in situ. Indeed, spectrin heterotetramers in intact cells have subsequently been estimated to be only 70 nm in length, based on experimentally determined values for the number of spectrin molecules and for the membrane surface area together with a plausible packing geometry (11). This estimate is consistent with quick-freeze, deep-etch rotary replication (QFDERR) and with atomic force microscopy (AFM) of intact, unexpanded skeletons, which revealed 30- to 50-nm-long filaments that were thought to represent spectrin heterotetramers. It is interesting to note that QFDERR revealed three or four spectrin attachments per junctional complex instead of five or six, suggesting that the skeletal network may undergo substantial reorganization as it expands into the single-layered form observed in negative stain (12–18).

In this study, we have utilized cryo-electron tomography (reviewed in Bárcena and Koster (19)) to reveal the three-dimensional architecture of the membrane skeleton from wild-type mice in a near-native environment. Specifically, these skeletons have been preserved in the frozen-hydrated

Submitted July 19, 2011, and accepted for publication September 27, 2011.

*Correspondence: stokes@nyu.edu

Editor: Edward Egelman.

0006-3495/11/11/2341/10 $2.00

doi: 10.1016/j.bpj.2011.09.050

state and have not been broken open by shear forces, thus avoiding artifacts due to heavy-metal contrasting agents, adsorption to substrates, and drying. In the resulting tomograms, spectrin filaments that would normally be obscured by the superimposition of cellular material are easily visualized as a convoluted, heterogeneous network. This has allowed us to characterize this network and to produce a model showing how it responds to shear stress.

MATERIALS AND METHODS

Membrane skeleton isolation

Erythrocytes were collected from adult wild-type mice under terminal anesthesia using cardiac puncture and added directly to anticoagulant acid citrate dextrose solution (0.15 ml/1 ml of blood). Membrane ghosts were prepared by hypotonic lysis, which involved placing them in 5 mM sodium phosphate buffer, pH 7.4, followed by three rounds of centrifugation and washing to remove residual hemoglobin (20). Membrane components were extracted by adding 2.5% Triton X-100 to the lysis buffer and incubating for 1 h on ice. This solution was layered on top of a discontinuous sucrose gradient (10%/60% sucrose in 0.1 mM sodium phosphate, pH 7.0), which was spun for 20 min at 100,000 $\times$ g at 4°C (8). Fractions were collected dropwise from the bottom of the tube and analyzed for protein content using UV absorption, refractive index, and SDS-PAGE (21). Peak fractions were used directly for negative staining or pooled and dialyzed overnight against 2 mM sodium phosphate, pH 7.4, for rapid freezing (see below). Western blots were carried out using antimouse or antirabbit secondary antibodies coupled to horseradish peroxidase and developed with an enhanced chemiluminescent detection kit according to published protocols (22).

Electron microscopy

For preparation of sheared skeletons, 200 mesh copper grids coated with carbon film containing 7 μm $\times$ 7 μm square holes (S 7/2, Quantifoil Micro Tools, Jena, Germany) were overlaid with a thin layer of continuous carbon (23) and glow-discharged. Skeletons were added at a concentration of 0.2 mg/ml and allowed to adsorb for 1 min. After blotting, they were either negatively stained with 1% uranyl acetate for 1 min or plunge-frozen. Negative staining resulted in spontaneous shearing of skeletons, but for frozen-hydrated samples, shearing was induced by a jet of buffer administered from a Pasteur pipette at a glancing angle immediately before blotting and freezing. For intact skeletons, 200 mesh molybdenum grids coated with a carbon film containing 5-μm-diameter round holes (R 5/20, Quantifoil) were made hydrophilic with a plasma cleaner (Solarus, Gatan, Pleasanton, CA) before use. Again, skeletons were added at 0.2 mg/ml and, after 1 min incubation, were simply blotted and plunge-frozen in a cold room. These frozen-hydrated samples were imaged over holes in the carbon film where no adsorption or shearing took place.

Electron tomography

For negatively stained samples, eight dual-axis tilt series were collected at 1° increments over a range of $\pm$70° using 2 μm defocus. Images were recorded with a Tecnai F20 electron microscope (FEI, Hillsboro, OR) equipped with a 4-K CCD camera (F415MP, TVIPS, Gauting, Germany) at a nominal magnification of 29,000 and a binning factor of 2, thus producing a pixel size of 5.9 Å. Alternatively, a CM200 electron microscope (FEI) equipped with a 1-K CCD camera (MSC1000, Gatan) was used at nominal magnifications of 27,500 or 50,000 (corresponding to pixel sizes of 6.5 Å or 3.6 Å). The total electron dose was ~4000 electrons/Å^2. Dual-axis tilt series were collected with a high-tilt tomography holder (model 916, Gatan). For the second tilt series about an orthogonal axis, the sample was manually rotated ~90° while outside the microscope, and the montage feature of SerialEM (24) was used to relocate the area of interest.

For intact frozen-hydrated samples, 13 single-axis tilt series were collected over a $\pm$66° range at 2° increments and a 9-μm defocus using SerialEM (24). A 3200FSC electron microscope (JEOL, Peabody, MA) equipped with an in-column energy filter and 4K CCD camera (UltraScan 4000, Gatan) was used at 30,000 nominal magnification and a binning factor of 2 (corresponding to a pixel size of 7.3 Å). The total electron dose was 70 electrons/Å^2. An energy window of 20 eV was used for zero-loss images and samples were kept at liquid nitrogen temperatures.

Image processing

Fiducial-free alignment of projection images and reconstruction of three-dimensional volumes was carried out using Protomo software (25). Data from dual-axis tilt series of negatively stained specimens were combined using IMOD (26,27). For visualizing tomograms of frozen-hydrated skeletons, nonlinear anisotropic diffusion was used to enhance contrast (28). Cross-correlational analysis was used to validate the identity of junctional complexes in the volume. For this analysis, a model of a 12-subunit actin filament was rendered at 4.2 nm resolution and systematically rotated and translated before cross correlation with the raw, unfiltered tomographic volume. After applying the appropriate missing wedge to the actin template, a series of three-dimensional maps of the cross-correlation coefficients was produced, and a final composite map was made, representing the highest cross-correlation coefficient at each voxel in the volume (29). Volume renderings of frozen-hydrated skeletons were generated using the Skeleton option found in the Amira 5.3 software package (Visage Imaging, San Diego, CA). Contour length measurements of junctional complexes along with spectrin heterotetramer dimensions and connectivity were calculated using IMOD (26,27) from the three cryo-electron tomograms with the best visibility (i.e., ice was thin and there were many filaments traceable throughout the volume).

RESULTS

Negatively stained membrane skeletons

For our electron tomography studies, membrane skeletons were prepared by extracting mouse red cell ghosts with Triton X-100, purifying them on a sucrose gradient, and then applying them directly to support films for either negative staining or rapid freezing. Consistent with previous work (7–10), membrane skeletons that were adsorbed to the carbon support film and negatively stained adopted a circular shape with a diameter of 10–12 μm. Because this diameter is more than twice that of the mature mouse red cell (5–6 μm), this preparation is thought to represent a stretched, or expanded, state of the skeleton (Fig. 1 *A*). Higher-magnification views of this expanded network reveal a latticelike arrangement of spectrin heterotetramers punctuated by junctional complexes (Fig. 1, *B* and *C*). An average length of 144 $\pm$ 26 nm (mean $\pm$ SD; range 86–187 nm, n = 64) indicates that many of the spectrin heterotetramers have been stretched close to their full contour length. Electron tomography confirms that the network is single-layered with 5.2 $\pm$ 0.7 (n = 35) spectrin heterodimer connections/junctional complex. A comparable result can be obtained with frozen-hydrated samples if the membrane

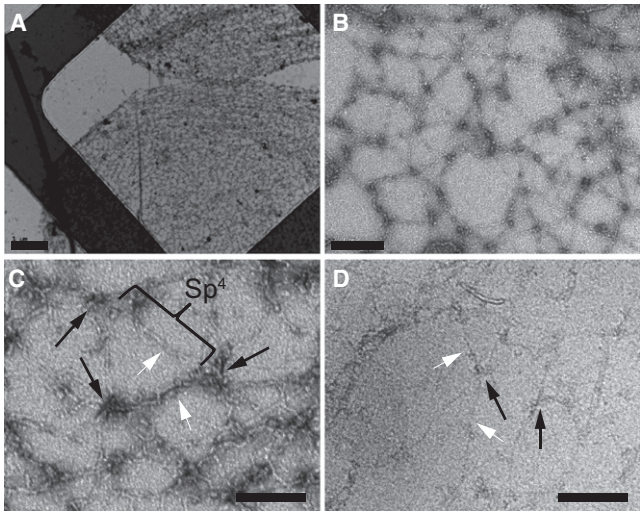

FIGURE 1 Negative-stain electron microscopy of the isolated, expanded erythrocyte membrane skeletons. (*A* and *B*) Low- (*A*) and medium-magnification (*B*) electron micrographs of membrane skeletons prepared by Triton X-100 extraction of mouse erythrocyte ghosts, which were adsorbed to carbon-coated grids and negatively stained. As a result of this procedure, the skeletons have been sheared open into a single layer. They have a diameter of ~10–12 μm, which is about twice as large as the mature mouse erythrocyte, indicating that the skeletons have been stretched. Scale bars, 1 μm (*A*) and 200 nm (*B*). (*C*) Higher-magnification view of the spread meshwork shows junctional complexes (*black arrows*) that are connected exclusively by spectrin heterotetramers (Sp^4) that had an average length of 144 nm (statistics were calculated from four double-tilt tomograms). Scale bar, 120 nm. (*D*) Cryo-electron micrograph of the expanded membrane skeleton. Skeletons were adsorbed to continuous carbon films and sheared with a jet of buffer before rapid freezing. Junctional complexes (*black arrows*) and spectrin filaments (*white arrowheads*) are clearly visible. The dimensions of these features are comparable to those in negatively stained samples. Scale bar, 120 nm.

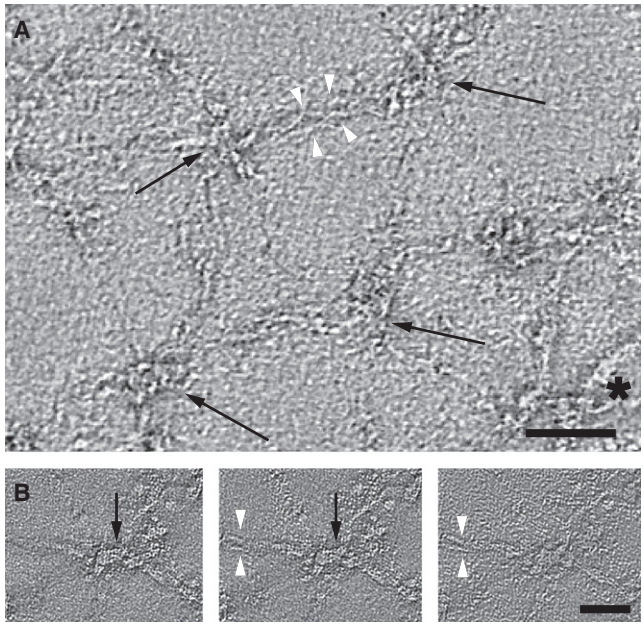

FIGURE 2 Negative-stain electron tomography of the expanded membrane skeleton. (*A*) Tomographic slice (5.9 Å thick) from a negatively stained, expanded membrane skeleton reveals junctional complexes (*black arrows*) and spectrin heterotetramers. Separation of the α- and β-spectrin molecules is sometimes visible distal to the junctional complexes (*white arrowheads*). Residual membrane fragments are occasionally present in the preparation (*asterisk*). Scale bar, 60 nm. (*B*) A series of high-magnification tomographic slices (3.6 Å thick) through a node in the spectrin network (*black arrow*) reveal a short (~30 nm), filamentous structure that corresponds to the junctional complex. This filamentous structure appears slightly bent, perhaps reflecting flexibility or distortion of F-actin at the junctional complex. Spectrin heterodimers are seen emanating from this complex and can be seen to bifurcate into individual α- and β-spectrin molecules ~50 nm away from the node (*white arrowheads*). The three individual *xy* slices shown are separated by 7 Å in the *z* direction. Scale bar, 45 nm.

skeletons are adsorbed to the carbon film and broken open with fluid shear before freezing (Fig. 1 *D*). We therefore conclude that shear forces, rather than the dehydration associated with the use of negative stain, are responsible for producing this expanded state.

Structural details of the filaments composing the negatively stained network are better visualized in tomograms from these samples (Fig. 2). Specifically, the expected short actin filaments at the junctional complexes can be measured to be ~30 nm in length. The spectrin filaments can be tracked, and in certain tomographic slices, they appear to splay apart, presumably reflecting a separation of α- and β-molecules that compose the heterodimer. It is interesting to note that these molecules become closely apposed as they approach the junctional complex. This observation provides direct evidence for a variability in the strength of lateral association between α- and β-spectrin, supporting previous analytical ultracentrifugation studies suggesting that heterodimer interactions are much stronger for spectrin repeats near the junctional complex ($\alpha_{21\text{-}20}$ and $\beta_{1\text{-}2}$) compared to other repeats more distal to the junctional complex (30).

Thickness and density of frozen-hydrated membrane skeletons

To evaluate the native architecture of the spectrin network, we used rapidly frozen preparations in which intact skeletons were suspended in vitrified buffer over holes in the carbon support film, thus eliminating both dehydration and adsorption to the carbon substrate and minimizing fluid shear (Fig. S1 in the Supporting Material). In contrast to the adsorbed skeletons, these intact, free-floating skeletons had a diameter similar to that of the mature mouse red cell (5–6 μm), suggesting that they retained their native shape. Consistent with previous QFDERR studies (12,15–17) and more recent AFM studies (13,14,18), tomograms representing 1.0–1.5 μm^2 areas at the skeleton edge reveal a densely packed, heterogeneous network of filaments coming from both the upper and lower layers of the membrane skeleton (Fig. 3 and Movie S1). At low magnification, these frozen-hydrated skeletons appear to have a smooth, circular shape (Fig. S1); however, higher-magnification tomographic slices show that the edge is in fact irregular

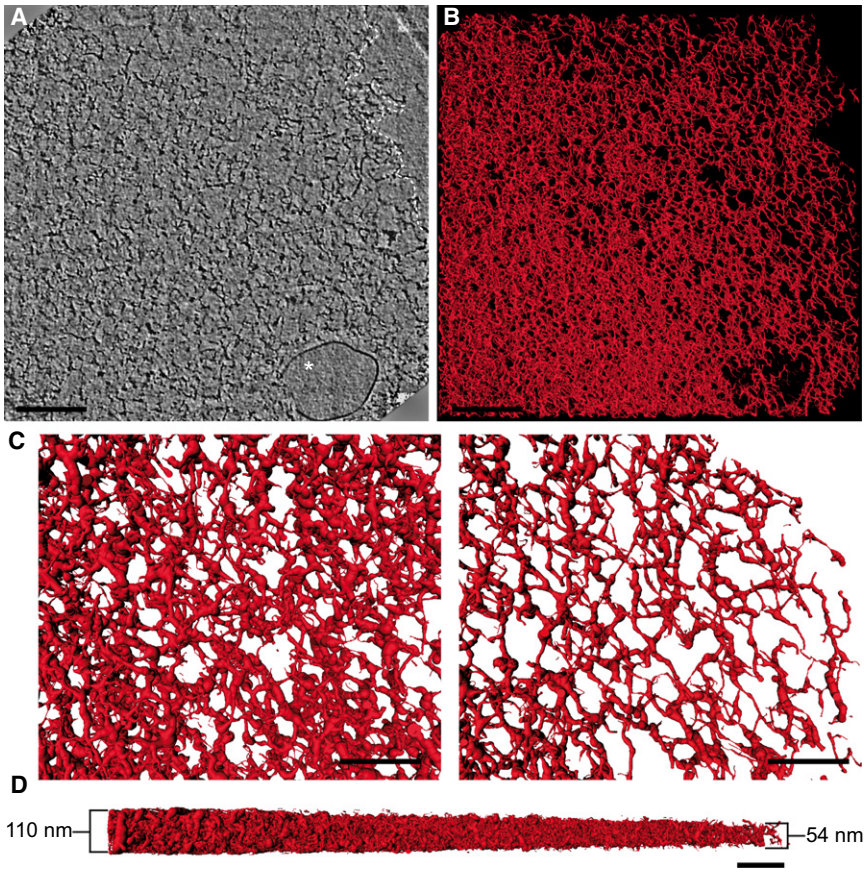

FIGURE 3 Cryo-electron tomography of the intact, unexpanded membrane cytoskeleton. Intact, unexpanded membrane skeletons derived from detergent-extracted mouse red cell ghosts were frozen and imaged over holes in the carbon substrate. (*A*) A 7.3-Å-thick slice from a tomogram collected from the edge of the skeleton (*white dashed line*) reveals a dense heterogeneous network of thin filaments. Residual membrane fragment is indicated by the white asterisk (see Movie S1). Scale bar, 200 nm. (*B*) Skeletonized volume-rendering of the intact membrane cytoskeleton shown in *A*. Note that filament density decreases from the center to the periphery of the skeleton (see Movie S2). Scale bar, 200 nm. (*C*) Close-up views of the network at the center (*left*) and edge (*right*) of the skeleton. Scale bar, 80 nm. (*D*) Side view of the volume-rendering from *B* showing that the overall thickness of the network decreases twofold over a distance of 1.5 μm. The average thickness of n = 12 skeletons (mean ± SD) was 110 ± 13 nm (range 88–128 nm) for the central region and 54 ± 9 nm (range 36–72 nm) at the edge. Scale bar, 100 nm.

(Fig. 3, *A* and *B*). Such irregularity probably results from compression of the skeleton into the thin layer required for vitrification (~150 nm), which will randomly fold the discrete filamentous network along its weak spots.

The surface density of filaments decreases from the center of the membrane skeleton to the edge, as illustrated by the volume rendering in Fig. 3 *C*. A similar gradient in the surface density of spectrin, protein 4.1, and actin has previously been associated with shear stress generated by aspirating erythrocyte membranes into micropipettes (31–34). In our case, this gradient may reflect a lateral force at the edge of the network due to its compression from plunge-freezing, and it illustrates how components of the skeleton are able to redistribute themselves in response to shear stress. The overall thickness of the membrane skeleton also increases from the edge of the cells (54 nm) to the center (110 nm) (Fig. 3 *D*), thus suggesting a coupling between surface density and membrane skeleton thickness.

Identification of spectrin filaments and junctional complexes

Unlike the hexagonal lattice of straight filaments that is seen in expanded skeletons (Fig. 1) (7–10), filaments in the tomograms from frozen-hydrated skeletons appear to be highly flexible, and their contour path varies from straight to sharply kinked (Fig. 4, *A* and *B*, and Movie S2). The diameters of interjunctional filaments are consistent with those of spectrin (4.0–4.5 nm (Fig. 4 *B*)), and their abundance is consistent with SDS-PAGE (Fig. S2 *A*), showing that α- and β-spectrin are the major components of isolated skeletons. The junctional complexes are distinguished by their high density, their larger diameter (8–9 nm) and shorter overall length, and the presence of multiple, thinner filaments emanating radially in various directions (Fig. 4, *A* and *C*). These visually identified junctional complexes also produced the highest cross-correlation coefficients when the tomographic volume was probed with an F-actin model (Fig. S3). Their average contour length of 27 ± 7 nm (Fig. 4 *D*) is consistent with an 8- to 12-monomer F-actin filament that composes the core of the junctional complex. This length is shorter than the 36.9 nm (13–14 actin monomers) previously measured from negatively stained samples (35). A possible explanation for the shorter length in our tomograms is that Mg^{2+}, which has previously been shown to lead to a loss of tropomyosin (36), was omitted during preparation of our membrane skeletons. Its 33-nm length is thought to provide a ruler for the length of F-actin filaments, thus constraining them to contain at least 12 monomers. However, in addition to tropomyosin,

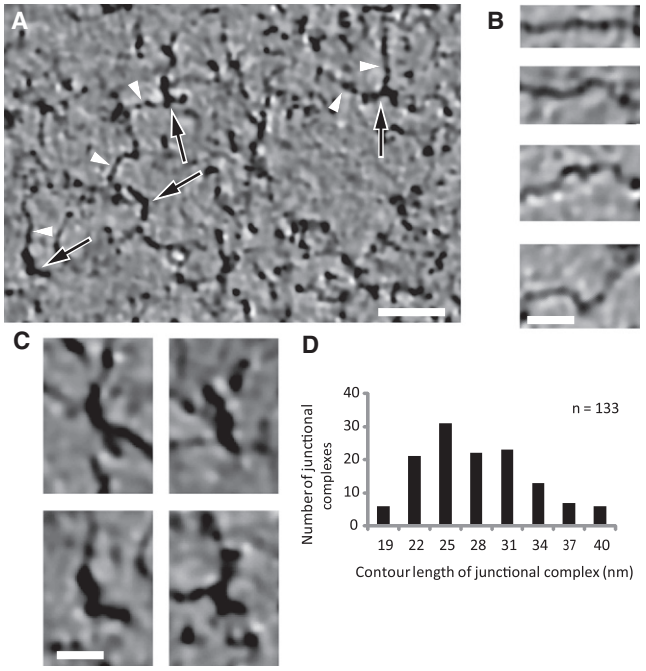

FIGURE 4 Identification of spectrin filaments and junctional complexes. (*A*) Tomographic slices reveal thin filaments (*white arrowheads*) with a diameter of 4.0–4.5 nm, which are consistent with the α/β-spectrin heterodimer. These filaments converge at nodes (*black arrows*), which have dimensions consistent with junctional complexes composed of protein 4.1, F-actin, and actin-binding proteins. Scale bar, 100 nm. (*B*) Gallery of spectrin filaments from tomographic slices, illustrating the variable shapes, ranging from relatively straight to sharply kinked. These particular examples were chosen to lie within a single tomographic slice, though typically the spectrin filaments will move in and out of multiple slices (see Movie S3). Scale bar, 20 nm. (*C*) Gallery of junctional complexes from tomographic slices characterized by a central density consistent with the size and shape of a short (30-nm) F-actin filament. These filaments were usually short and straight (*upper*), but a small number were distinctly bent (*lower*), as also observed in the expanded skeleton in Fig. 2 *B*. (*D*) Histogram of contour lengths for the junctional complex. The average of 27 ± 7 nm (mean ± SD; range 17–37 nm; n = 133) is consistent with an F-actin molecule of 8–12 monomers.

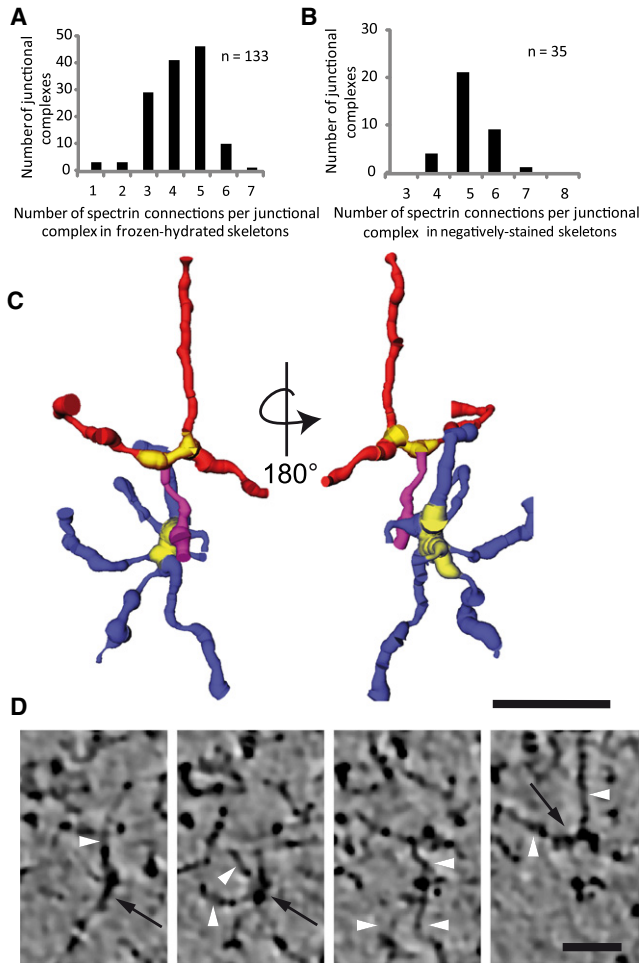

FIGURE 5 Three-dimensional topology of the membrane skeleton. (*A* and *B*) Histogram of the number of spectrin connections per junctional complex for frozen-hydrated and negatively stained skeletons, respectively. For frozen-hydrated skeletons, the mean ± SD of spectrin connections/junctional complex was 4.2 ± 1.0 (range 1–6, n = 133). For negatively stained skeletons, the mean ± SD was 5.2 ± 0.7 nm (range 4–7 nm, n = 35). (*C*) Skeletonized, volume-rendering of two junctional complexes (*yellow*) with their associated spectrin filaments (*red* and *blue*). A spectrin heterotetramer connecting the two junctional complexes is highlighted in magenta. The two views are related by a 180° rotation. Scale bar, 50 nm. (*D*) Tomographic slices at intervals of 9 nm through these same junctional complexes (*black arrows*), showing the spectrin filaments (*white arrowheads*). Scale bar, 35 nm. Also see Movie S3 and another example of local network topology in Fig. S4.

tropomodulin and adducin act as capping proteins that are also important for maintaining actin filament length (35). It should be noted that Western blots from our preparations demonstrated the presence of tropomyosin, together with other major and minor constituents of the junctional complex (actin by SDS-PAGE, protein 4.1, and tropomodulin by Western blot) (Fig. S2 *B*), suggesting that our membrane skeletons were fundamentally intact.

Three-dimensional topology of the skeleton

The number of spectrin heterodimers attached to each junctional complex represents an important parameter governing the mechanical properties of the membrane skeleton. From three-dimensional analysis of our tomograms, we typically observed three, four, or five spectrins connected to a given junctional complex, and only rarely six (Fig. 5, Fig. S4, and Movie S3). On average, we measured 4.2 ± 1.0 (n = 133) spectrin heterodimers per junctional complex, which is consistent with estimates from QFDERR and AFM studies (12–17), but less than the 5.2 ± 0.7 (n = 35) measured from our negatively stained, expanded skeletons (Fig. 5 *B*). However, the convoluted path of spectrin, the dense organization of the network, and the low signal/noise ratio in the tomograms makes it difficult to precisely identify every spectrin heterodimer emanating from a given junctional complex, and the value of 4.2 may therefore be a slight underestimate.

The spectrin heterotetramer is a flexible molecule that is 194 nm long in the fully extended state (6) but has been predicted to be only 70–80 nm in a cellular context (11,37). In our tomographic reconstructions, the contour length of the spectrin heterotetramer is 46 ± 15 nm (n = 130) (Fig. 6), which is also comparable to measurements from QFDEER and AFM images (12–17). To our surprise, despite the observed gradient in skeleton thickness and in filament density (Fig. 3), we found that the contour length of spectrin heterotetramers did not vary significantly across the cell. Thus, the higher surface density of junctional complexes at the center of the cell seems to be achieved by spectrin following a more convoluted path between the nodes rather than by any change in the spectrin contour length. Comparison with the expanded network produced from these same samples and shown in Fig. 1 indicates that expansion was not simply due to prolonged incubation in buffer of low ionic strength; more likely, adsorption to the carbon film combined with blotting to produce relatively high levels of fluid shear during the preparation of samples for electron microscopy.

Oligomeric state of spectrin

In conventional models of the membrane skeleton, spectrin filaments are depicted as heterotetramers, consisting of two heterodimers of α- and β-spectrin that are connected head-to-head to produce a bipolar filament. However, there have been reports of higher-order oligomers, and our tomograms provide the first, to our knowledge, direct view of hexameric and octameric spectrin in an intact membrane skeleton. Specifically, spectrin heterotetramers were readily identified in our tomograms as linear filaments running between junctional complexes, but we also observed a plethora of branched filaments that were either Y-shaped or cross-shaped and that terminated in nearby junctional complexes (Fig. 7, *A* and *B*). These branched structures appear similar to the polyskelions observed in rotary shadowed preparations of isolated spectrin (38) and presumably represent hexamers and octamers, respectively. Accordingly, our networks appeared to be composed of a stochastic combination of tetramers, hexamers, and octamers connecting each pair of junctional complexes (Fig. 7, *C* and *D*, and Movie S4). Although we did not quantify their relative abundance, higher-order oligomers were observed spanning virtually every pair of nodes in the network.

DISCUSSION

By using cryo-electron tomography to image intact membrane skeletons from red cells, we have, to our knowledge, produced the first truly three-dimensional structure of this oft-studied macromolecular assembly. The skeletons comprise a dense, convoluted network of spectrin filaments connecting to actin filaments at the junctional complexes. Both the surface density of the network and its overall thickness were lower at the edge of the cell compared to the middle. Three-dimensional tracking of individual spectrin

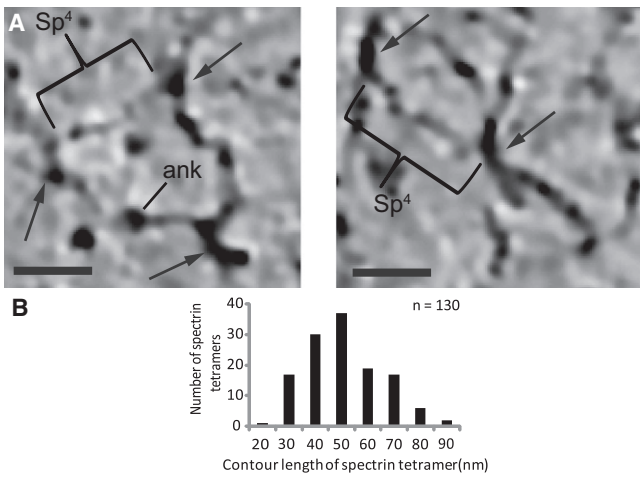

FIGURE 6 Spectrin heterotetramer dimensions. (*A*) Two examples of junctional complexes (*black arrows*) connected by spectrin heterotetramers (Sp^4). Because these are thin tomographic slices, the spectrin molecules tend to leave the plane of the slice and junctional complexes have variable appearances depending on their orientation. A putative ankyrin molecule (ank), which binds to the 15th repeat of β-spectrin, is indicated at the expected position halfway between junctional complexes (8,50). Scale bars, 25 nm. (*B*) Histogram of contour lengths of the spectrin tetramers shows an average of 46 ± 15 nm (mean ± SD; range 19–97 nm, n = 130). When separated into two groups corresponding to the center and edge of the cell, there was no significant difference in this length: center, 45.8 ± 2.3 nm; edge, 46.2 ± 2.3 nm (mean ± SE; p = 0.9809).

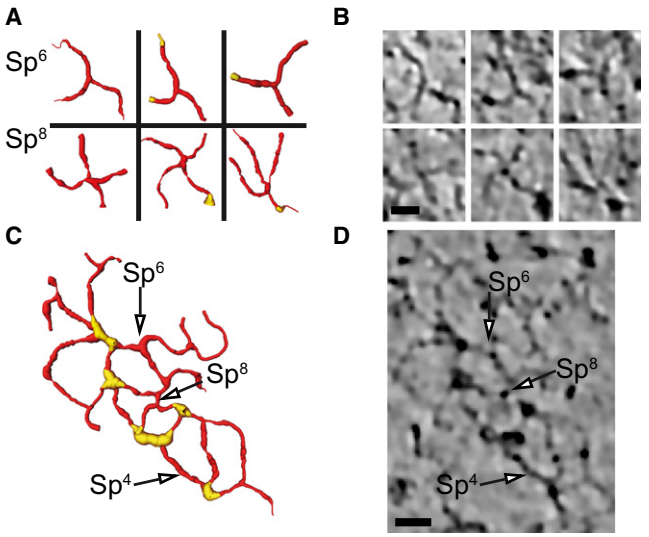

FIGURE 7 Oligomeric state of spectrin. (*A*) Gallery of skeletonized volume-renderings of spectrin hexamers (*upper*) and octamers (*lower*) extracted from the tomograms. Junctional complexes are highlighted in yellow. (*B*) Corresponding tomographic slices through the oligomers shown in *A*. (*C*) Skeletonized volume-rendering of a region of the cytoskeleton, illustrating junctional complexes (*yellow*) connected by spectrin heterotetramers (Sp^4), hexamers (Sp^6), and octamers (Sp^8). (*D*) Tomographic slice through the corresponding region of the tomogram. Scale bars, 20 nm.

heterotetramers indicated that their contour length averages 46 ± 15 nm, indicating that spectrin filaments are only approximately one-quarter of the full contour length of the extended heterotetramer in situ. In addition to the linear, tetrameric form, we observed a large proportion of branched spectrin oligomers, such as hexamers and octamers, connecting junctional complexes.

Thickness and topology of the membrane skeleton

Our measurements of the membrane skeleton thickness indicate a twofold change across the cell—from 54 nm at the cell edge to 110 nm at the center—which could be explained by a corresponding gradient in membrane stress. Indeed, previous measurements with force probes and interferometry (39) indicated that the entire membrane assembly could be compressed by a factor of 1.8 in cells under ~100 pN of force. In a similar way, blotting of our samples before plunge-freezing will compress the skeletons, thus producing high curvature at the cell edges and localized lateral stress similar to that experienced by the red cell in circulation. To compare our measurements of isolated skeletons with those involving the entire membrane-bound skeleton, we can add 10 nm for the space between the junctional complex and the lipid bilayer (40), 4 nm for the lipid bilayer itself, and 6 nm for the glycocalyx (41). Based on these values and the fact that our tomograms represent two juxtaposed skeletons, we estimate the overall thickness for the membrane-bound assembly to be 47 nm at the edge and 75 nm in the middle of cells. The value of 47 nm is indeed consistent with both the 40–50 nm measured by Heinrich et al. for cells under stress (39) and the 42 ± 15 nm measured by Hategan et al. using AFM (18). However, our estimated thickness at the center of the cells (75 nm) is somewhat less than the 90 nm measured by force probes on unstressed cells (39), indicating that the cell centers may also experience stress during sample preparation for electron microscopy, albeit less than at the edge. In any case, our observation of a concomitant gradient in thickness and in surface density of filaments is consistent with the idea that changes in filament density represent a key response to membrane stress.

Although the resolution of our reconstructions is too low to evaluate the secondary and tertiary structures of spectrin, our observations of the dimensions of spectrin heterotetramers (46 nm in length and 4.5 nm in diameter) can be considered in light of several models that attempt to explain the molecular basis for its flexibility. X-ray crystal structures of two tandem α-spectrin repeats led to suggestions that a loop-to-helix transition within the spectrin repeat, or bending at the linker between repeats, can induce supercoiling of the heterodimer. A model including a combination of these effects was shown to reduce the linear end-to-end extent of spectrin by two-thirds (42). The inflective and kinked shapes of spectrin in our tomograms are generally consistent with this model, though the model does not explain the reduced contour length seen in our tomograms. Reductions in contour length could be explained by another model positing that flexibility at the linker region allows individual triple-helical spectrin repeats to fold back upon themselves (43). However, our reconstructions do not show the implied heterogeneity in the diameter of spectrin heterodimers (Fig. 4 *B*), which would increase from 4.5 to ~7 nm in the folded state. Alternatively, Fourier-filtered images of negatively stained spectrin from expanded membrane skeletons suggest supercoiling of spectrin heterodimers (9), though it is not clear whether this could reduce contour length enough to account for the 46-nm length of spectrin heterotetramers seen in our tomograms.

Oligomeric state of spectrin

Our tomograms provide the first direct view of branched hexameric and octameric spectrin filaments in an intact membrane skeleton. Like the heterotetramer, assembly of these oligomers is likely mediated by a swapping of α- and β-strands, except that the α- and β-strands from a given heterodimer would make three- or four-way junctions with different neighboring α- and β-strands (Fig. 8 *C*) (44–46). In previous studies, hexamers were observed in negatively stained membrane skeletons and were estimated to account for ~11% of the total spectrin (8). In a similar way, QFDERR was used to image antibodies to the head region of α-spectrin, thus revealing intersections between three or four spectrin filaments (16). In both QFDERR and rotary-shadowing studies of isolated spectrin purified from red cell extracts, such oligomers were estimated to account for 25–35% of total spectrin (38). Although we could not establish a reliable fraction given the difficulty in accurately tracking every spectrin molecule through the tomograms, oligomers were seen between virtually every junctional complex in our tomograms, and our observations are therefore consistent with the higher estimates for their prevalence.

Model for intact membrane skeleton and conversion to the expanded form

Comparisons between our images of sheared and intact skeletons suggest that formation of specific spectrin oligomers is transient and that remodeling of these oligomers may constitute the network's response to stress. In contrast to the network observed in intact, free-floating skeletons (Fig. 7), adsorption and shearing of skeletons results in a lower density of junctional complexes and a predominance of fully extended spectrin tetramers (Figs. 1 and 2). This result suggests that the oligomeric state of spectrin is in a dynamic equilibrium and may be a determining factor in the flexibility of the red-cell membrane as a whole. Assuming a concentration dependence for oligomerization, the large

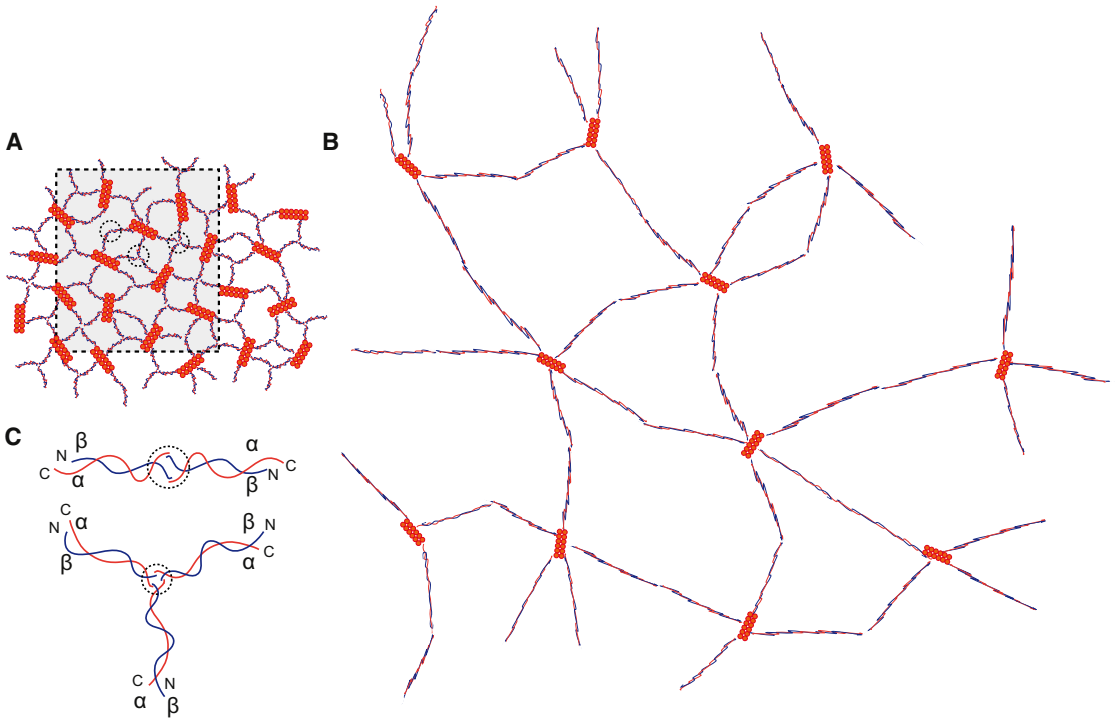

FIGURE 8 Model for transition between the intact and expanded forms of the erythrocyte membrane skeleton. (*A*) Our model of the unexpanded membrane skeleton, which is consistent with cryo-electron tomography of frozen-hydrated preparations of intact skeletons. This model is composed of spectrin molecules (*thin red and blue strands*) connecting junctional complexes (*orange filaments*). Spectrin heterodimers composed of α- (*red*) and β (*blue*)-chains are connected to each junctional complex. Higher-order tetramers, hexamers, and octamers are formed by self-association sites halfway between the junctional complexes (*circles*). Our data suggest that these self-association sites are transient and that coupling between individual spectrin molecules is continually being reconfigured. (*B*) Model of the expanded skeleton that is consistent with electron tomography of sheared skeletons that were adsorbed to the carbon support. This model represents an expansion of the boxed region in *A* and is drawn at the same scale. Expansion produces a lower surface density of spectrin molecules, which we believe accounts for the observed shift of higher-order spectrin oligomers (hexamers and octamers) toward the tetrameric form, which is fully extended. Thus, the dynamic equilibrium of the spectrin network allows the erythrocyte to undergo large deformations in response to shear force. (*C*) Schematic representations of a spectrin heterotetramer (*upper*) and hexamer (*lower*). Heterotetramers are formed through an exchange of α-helices from the N- and C-termini of α- and β-spectrin, respectively (overlap of chains inside the circle). Higher-order oligomers, such as hexamers and octamers, can be formed in a similar manner, except that the α- and β-spectrin molecules pair with α- and β-spectrin molecules that originate from different heterodimers.

fraction of higher-order oligomers observed in intact skeletons could reflect an innate overabundance of spectrin relative to the surface area of the relaxed red cell (44,47). Thus, local regions of the network would be poised to convert the higher order oligomers into heterotetramers or even into unassociated heterodimers, thus allowing this region of the membrane to stretch during red cell deformation (Fig. 8). Indeed, the dynamic nature of spectrin oligomerization is supported by the ready incorporation of peptides from the N-terminus of α-spectrin into the network in situ (48). There is also evidence that localized unfolding of spectrin chains contributes to elasticity, as shown by the incorporation of cysteine labels along the length of the spectrin heterodimer in response to shear stress (49). Finally, it is notable that the red cell disorders of hereditary elliptocytosis and pyropoikilocytosis, where cells fail to return to their resting biconcave disc shape, are characterized by mutations in the head-to-head oligomerization site of spectrin, which could very well impact the stability of oligomers (1,5).

CONCLUSION

In summary, we have used cryo-electron tomography to characterize the architecture of the erythrocyte membrane skeleton in the native state. Our three-dimensional volumes show that the membrane skeleton is composed of a heterogeneous network of spectrin oligomers that follow convoluted paths to link the junctional complexes together. The thickness of the skeleton and the surface density of the spectrin network vary across the cell and appear to be coupled to the level of membrane stress. We observed a significant fraction of hexameric and octameric spectrin assemblies and propose that the interconversion of spectrin oligomers is dynamic, thus facilitating the extreme deformations that the red cell undergoes throughout its life cycle.

SUPPORTING MATERIAL

Four figures and four movies are available at http://www.biophysj.org/biophysj/supplemental/S0006-3495(11)01181-7.

Electron microscopy was conducted with the facilities at the New York Structural Biology Center, and we thank Ruben Diaz and Bill Rice for their assistance with the JEOL-3200 electron microscope. We also thank Natalya Gertsik for her generous help with membrane skeleton isolation, Xuili An and Alejandra Leo-Macias for helpful discussions, and Salvatore Valvo for assistance with mice.

The JEOL-3200 electron microscope was purchased with funds from National Institutes of Health grant S10 RR17291. Support for this work was provided by the New York University Structural Biology Graduate program and National Institutes of Health grant F31NS056467 to A.N. Representative tomograms have been deposited in the Electron Microscopy Data Bank (accession code EMD-1967).

REFERENCES

1. Mohandas, N., and E. Evans. 1994. Mechanical properties of the red cell membrane in relation to molecular structure and genetic defects. *Annu. Rev. Biophys. Biomol. Struct.* 23:787–818.
2. Mohandas, N., and P. G. Gallagher. 2008. Red cell membrane: past, present, and future. *Blood.* 112:3939–3948.
3. Chasis, J. A., and N. Mohandas. 1986. Erythrocyte membrane deformability and stability: two distinct membrane properties that are independently regulated by skeletal protein associations. *J. Cell Biol.* 103:343–350.
4. Bennett, V., and A. J. Baines. 2001. Spectrin and ankyrin-based pathways: metazoan inventions for integrating cells into tissues. *Physiol. Rev.* 81:1353–1392.
5. An, X., and N. Mohandas. 2008. Disorders of red cell membrane. *Br. J. Haematol.* 141:367–375.
6. Shotton, D. M., B. E. Burke, and D. Branton. 1979. The molecular structure of human erythrocyte spectrin. Biophysical and electron microscopic studies. *J. Mol. Biol.* 131:303–329.
7. Byers, T. J., and D. Branton. 1985. Visualization of the protein associations in the erythrocyte membrane skeleton. *Proc. Natl. Acad. Sci. USA.* 82:6153–6157.
8. Liu, S. C., L. H. Derick, and J. Palek. 1987. Visualization of the hexagonal lattice in the erythrocyte membrane skeleton. *J. Cell Biol.* 104:527–536.
9. McGough, A. M., and R. Josephs. 1990. On the structure of erythrocyte spectrin in partially expanded membrane skeletons. *Proc. Natl. Acad. Sci. USA.* 87:5208–5212.
10. Shen, B. W., R. Josephs, and T. L. Steck. 1986. Ultrastructure of the intact skeleton of the human erythrocyte membrane. *J. Cell Biol.* 102:997–1006.
11. Steck, T. L. 1989. Red cell shape. *In* Cell Shape: Determinants, Regulation, and Regulatory Role. W. D. Stein and F. Bronner, editors. Academic, San Diego. 205–246.
12. Ohno, S., N. Terada, …, H. Ueda. 1994. Membrane skeleton in fresh unfixed erythrocytes as revealed by a rapid-freezing and deep-etching method. *J. Anat.* 185:415–420.
13. Swihart, A. H., J. M. Mikrut, …, R. C. Macdonald. 2001. Atomic force microscopy of the erythrocyte membrane skeleton. *J. Microsc.* 204:212–225.
14. Takeuchi, M., H. Miyamoto, …, A. Kusumi. 1998. Structure of the erythrocyte membrane skeleton as observed by atomic force microscopy. *Biophys. J.* 74:2171–2183.
15. Terada, N., Y. Fujii, and S. Ohno. 1996. Three-dimensional ultrastructure of in situ membrane skeletons in human erythrocytes by quick-freezing and deep-etching method. *Histol. Histopathol.* 11:787–800.
16. Ursitti, J. A., D. W. Pumplin, …, R. J. Bloch. 1991. Ultrastructure of the human erythrocyte cytoskeleton and its attachment to the membrane. *Cell Motil. Cytoskeleton.* 19:227–243.
17. Ursitti, J. A., and J. B. Wade. 1993. Ultrastructure and immunocytochemistry of the isolated human erythrocyte membrane skeleton. *Cell Motil. Cytoskeleton.* 25:30–42.
18. Hategan, A., R. Law, …, D. E. Discher. 2003. Adhesively-tensed cell membranes: lysis kinetics and atomic force microscopy probing. *Biophys. J.* 85:2746–2759.
19. Bárcena, M., and A. J. Koster. 2009. Electron tomography in life science. *Semin. Cell Dev. Biol.* 20:920–930.
20. Dodge, J. T., C. Mitchell, and D. J. Hanahan. 1963. The preparation and chemical characteristics of hemoglobin-free ghosts of human erythrocytes. *Arch. Biochem. Biophys.* 100:119–130.
21. Fairbanks, G., T. L. Steck, and D. F. Wallach. 1971. Electrophoretic analysis of the major polypeptides of the human erythrocyte membrane. *Biochemistry.* 10:2606–2617.
22. An, X., M. Salomao, …, N. Mohandas. 2007. Tropomyosin modulates erythrocyte membrane stability. *Blood.* 109:1284–1288.
23. Grassucci, R. A., D. J. Taylor, and J. Frank. 2007. Preparation of macromolecular complexes for cryo-electron microscopy. *Nat. Protoc.* 2:3239–3246.
24. Mastronarde, D. N. 2005. Automated electron microscope tomography using robust prediction of specimen movements. *J. Struct. Biol.* 152: 36–51.
25. Winkler, H., and K. A. Taylor. 2006. Accurate marker-free alignment with simultaneous geometry determination and reconstruction of tilt series in electron tomography. *Ultramicroscopy.* 106:240–254.
26. Kremer, J. R., D. N. Mastronarde, and J. R. McIntosh. 1996. Computer visualization of three-dimensional image data using IMOD. *J. Struct. Biol.* 116:71–76.
27. Mastronarde, D. N. 1997. Dual-axis tomography: an approach with alignment methods that preserve resolution. *J. Struct. Biol.* 120: 343–352.
28. Frangakis, A. S., and R. Hegerl. 2001. Noise reduction in electron tomographic reconstructions using nonlinear anisotropic diffusion. *J. Struct. Biol.* 135:239–250.
29. Bohm, J., A. S. Frangakis, …, W. Baumeister. 2000. Toward detecting and identifying macromolecules in a cellular context: template matching applied to electron tomograms. *Proc. Natl. Acad. Sci. USA.* 97:14245–14250.
30. Begg, G. E., S. L. Harper, …, D. W. Speicher. 2000. Initiation of spectrin dimerization involves complementary electrostatic interactions between paired triple-helical bundles. *J. Biol. Chem.* 275:3279–3287.
31. Discher, D. E., D. H. Boal, and S. K. Boey. 1998. Simulations of the erythrocyte cytoskeleton at large deformation. II. Micropipette aspiration. *Biophys. J.* 75:1584–1597.
32. Discher, D. E., and N. Mohandas. 1996. Kinematics of red cell aspiration by fluorescence-imaged microdeformation. *Biophys. J.* 71:1680–1694.
33. Discher, D. E., N. Mohandas, and E. A. Evans. 1994. Molecular maps of red cell deformation: hidden elasticity and in situ connectivity. *Science.* 266:1032–1035.
34. Lee, J. C., D. T. Wong, and D. E. Discher. 1999. Direct measures of large, anisotropic strains in deformation of the erythrocyte cytoskeleton. *Biophys. J.* 77:853–864.
35. Moyer, J. D., R. B. Nowak, …, V. M. Fowler. 2010. Tropomodulin 1-null mice have a mild spherocytic elliptocytosis with appearance of tropomodulin 3 in red blood cells and disruption of the membrane skeleton. *Blood.* 116:2590–2599.
36. Fowler, V. M., and V. Bennett. 1984. Erythrocyte membrane tropomyosin. Purification and properties. *J. Biol. Chem.* 259:5978–5989.
37. Stokke, B. T., A. Mikkelsen, and A. Elgsaeter. 1985. Human erythrocyte spectrin dimer intrinsic viscosity: temperature dependence and implications for the molecular basis of the erythrocyte membrane free energy. *Biochim. Biophys. Acta.* 816:102–110.
38. Liu, S. C., P. Windisch, …, J. Palek. 1984. Oligomeric states of spectrin in normal erythrocyte membranes: biochemical and electron microscopic studies. *Cell.* 37:587–594.
39. Heinrich, V., K. Ritchie, …, E. Evans. 2001. Elastic thickness compressibilty of the red cell membrane. *Biophys. J.* 81:1452–1463.

40. Shahrokh, Z., A. S. Verkman, and S. B. Shohet. 1991. Distance between skeletal protein 4.1 and the erythrocyte membrane bilayer measured by resonance energy transfer. *J. Biol. Chem.* 266:12082–12089.

41. Linss, W., C. Pilgrim, and H. Feuerstein. 1991. How thick is the glycocalyx of human erythrocytes? *Acta Histochem.* 91:101–104.

42. Grum, V. L., D. Li, …, A. Mondragón. 1999. Structures of two repeats of spectrin suggest models of flexibility. *Cell.* 98:523–535.

43. Bloch, R. J., and D. W. Pumplin. 1992. A model of spectrin as a concertina in the erythrocyte membrane skeleton. *Trends Cell Biol.* 2:186–189.

44. Morrow, J. S., and V. T. Marchesi. 1981. Self-assembly of spectrin oligomers in vitro: a basis for a dynamic cytoskeleton. *J. Cell Biol.* 88:463–468.

45. Morrow, J. S., W. B. Haigh, Jr., and V. T. Marchesi. 1981. Spectrin oligomers: a structural feature of the erythrocyte cytoskeleton. *J. Supramol. Struct. Cell. Biochem.* 17:275–287.

46. Morrow, J. S., D. W. Speicher, …, V. T. Marchesi. 1980. Identification of functional domains of human erythrocyte spectrin. *Proc. Natl. Acad. Sci. USA*. 77:6592–6596.

47. Morrow, J. S., and W. B. Haigh, Jr. 1983. Erythrocyte membrane proteins: detection of spectrin oligomers by gel electrophoresis. *Methods Enzymol.* 96:298–304.

48. An, X., M. C. Lecomte, …, W. Gratzer. 2002. Shear-response of the spectrin dimer-tetramer equilibrium in the red blood cell membrane. *J. Biol. Chem.* 277:31796–31800.

49. Krieger, C. C., X. An, …, D. E. Discher. 2011. Cysteine shotgun-mass spectrometry (CS-MS) reveals dynamic sequence of protein structure changes within mutant and stressed cells. *Proc. Natl. Acad. Sci. USA*. 108:8269–8274.

50. Kennedy, S. P., S. L. Warren, …, J. S. Morrow. 1991. Ankyrin binds to the 15th repetitive unit of erythroid and nonerythroid β-spectrin. *J. Cell Biol.* 115:267–277.